

## OUTFLOWS AND HOT DUST EMISSION

---

### 1.1 INTRODUCTION

Many quasars and AGNs show an excess in their near-infrared continuum emission. This feature is generally attributed to thermal emission from dust heated by optical/ultra-violet radiation from the accretion disc. The wavelength of the feature ( $\sim 2 \mu\text{m}$ ) corresponds to the spectral peak for graphite dust at its sublimation temperature ( $T \sim 1500 \text{ K}$ ; Barvainis, 1987). Reverberation measurements of nearby AGNs suggest that the hot dust is very close to the central source (few tens of light days; e.g. Minezaki et al., 2004; Suganuma et al., 2006). This places the dust at the innermost edge of the putative torus-like structure, at a radius set by the sublimation temperature of the dust grains.

Studies have fitted the near-infrared SEDs of AGNs using a blackbody spectrum to represent emission from hot dust (e.g. Edelson and Malkan, 1986; Barvainis, 1987; Kishimoto et al., 2007; Mor, Netzer, and Elitzur, 2009; Riffel, Storchi-Bergmann, and McGregor, 2009; Deo et al., 2011; Landt et al., 2011; Mor and Trakhtenbrot, 2011; Roseboom et al., 2013). A hot dust component is present in the vast majority of AGNs, although populations of ‘dust-free’ objects have also been discovered (Hao et al., 2010; Hao et al., 2011; Jiang et al., 2010; Mor and Trakhtenbrot, 2011). It is not yet clear how the hot dust properties relate to other AGN properties such as BH mass, luminosity and accretion rate.

In recent years the picture of the torus has evolved away from a static ‘doughnut’ towards a more general circum-nuclear, geometrically and optically thick dust distribution. As we have previously discussed (e.g. Section ??), winds and outflows launched from the accretion disc are very common in AGN. In the dusty wind model - first proposed by Konigl and Kartje, (1994) and later developed by, amongst others, Everett, (2005), Elitzur and Shlosman, (2006), Keating et al., (2012) - the torus is the dusty part of an accretion disc wind beyond the dust sublimation radius. The dusty clouds are uplifted above the disc where they are directly exposed to the central engine. The

dust is heated, and radiates in the near-infrared band. At the same time, radiation pressure due to dust can efficiently accelerate the wind. The wind is roughly polar, and so naturally provides circum-nuclear obscuration around the accretion disc and dust-free BLR. This model is supported by recent interferometric observations of nearby Seyfert galaxies which find that the mid-infrared emission is dominated by dust in the polar regions (e.g. Raban et al., 2009; Hönig et al., 2012; Hönig et al., 2013; Tristram et al., 2014; López-Gonzaga et al., 2016).

Studying the relationship between emission from hot dust and outflow diagnostics in the BLR can help place constraints on this dusty wind model (e.g. Wang et al., 2013). This is now possible by combining data from the SDSS spectroscopic and photometric surveys with photometric surveys such as UKIDSS and WISE. At redshifts  $2 \lesssim z \lesssim 3$ , SDSS spectra reveal BH masses, accretion rates and diagnostics of the BLR dynamics. At the same time, the available photometric data provides full UV to infrared rest-frame coverage of the SED. In particular, the WISE photometry is sensitive to the  $3 \mu\text{m}$  region of the SED which is dominated by hot dust.

In this Chapter we build a simple parametric SED model that is able to reproduce the median optical-infrared colours of tens of thousands of SDSS AGN at redshifts  $1 \lesssim z \lesssim 3$  (Section ). We use this model to measure the hot dust properties of a large sample of  $2 < z < 2.7$  quasars for which we have already measured C iv line properties, BH masses and Eddington ratios (Section 1.6).

## 1.2 DATA

### 1.2.1 SDSS

We use spectroscopic data from the Seventh Data Release (DR7) of the SDSS spectroscopic quasar catalogue (Schneider et al., 2010). The SDSS photometric survey obtained images in five broad optical passbands: u, g, r, i and z (Table 1.1). We use BEST point-spread function magnitudes from the SDSS DR7 quasar catalogue.

#### *UKIDSS Large Area Survey*

We use the tenth data release (DR10) of the UKIRT Infrared Deep Sky Survey (UKIDSS; Lawrence et al., 2007) Large Area

Survey	Passband	$\lambda_{\text{eff}}$ [ $\mu\text{m}$ ]	AB offset	$A_{\text{filter}}/E(B - V)$
SDSS	u	0.3543	0.913	4.875
	g	0.4770	-0.081	3.793
	r	0.6231	0.169	2.721
	i	0.7625	0.383	2.099
	z	0.9134	0.542	1.537
UKIDSS	Y	1.0305	0.641	1.194
	J	1.2483	0.941	0.880
	H	1.6313	1.378	0.569
	K	2.2010	1.897	0.352
WISE	W1	3.4	2.691	0.182
	W2	4.6	3.331	0.130
	W3	12.0		

Table 1.1: Available photometry, effective wavelength, Vega to AB magnitude offsets, conversion from  $E(B - V)$  to extinction.   
Need W3 offset/ extinction. Ask Paul or just use WISE values/zero.

Survey (ULAS) which has observed  $\sim 3,200 \text{ deg}^2$  in four near-infrared passbands: Y, J, H and K. We use ‘apermag3’ magnitudes, which are aperture corrected magnitudes in a  $2''$  diameter aperture.

#### WISE All-WISE Survey

The Wide-field Infrared Explorer (WISE; Wright et al., 2010) mapped the entire sky in four mid-IR passbands: W1, W2, W3 and W4. The WISE AllWISE Data Release (‘AllWISE’) combines data from the nine-month cryogenic phase of the mission that led to the ‘AllSky’ data release with data from the NEOWISE program (Mainzer et al., 2011). We use the profile-fitting ‘mpro’ magnitudes. Only information from the first three WISE passbands are used in this work.

#### 1.2.2 Computing Vega-AB magnitude offsets

Vega magnitudes are used throughout this Chapter. This is the native magnitude system for UKIDSS and WISE. We add 0.08 mag to the UKIDSS Y passband magnitudes to bring the photometry into better agreement with the SDSS z and UKIDSS J photometry. SDSS uses an ‘asinh’ magnitude system (Lupton, Gunn, and Szalay, 1999) which is intended to be on the AB

system (Oke and Gunn, 1983). However, the photometric zero-points are known to be slightly off the AB standard. The  $z$  passband is in error by 0.02 ( $z_{AB} = z_{SDSS} + 0.02$ )<sup>1</sup>. The  $u$  passband was in error by 0.04 dex at the time of DR7. However, using an updated  $u$  throughput function, we find that the  $u$  zero-point is now consistent with the AB system.

Using a reference template, we calculate the AB magnitude of Vega in each passband (Table 1.1). The mean flux density  $f_\lambda(P)$  in a passband defined by a throughput function  $P(\lambda)$  is given by:

$$f_\lambda(P) = \frac{\int P(\lambda) f_\lambda(\lambda) \lambda d\lambda}{\int P(\lambda) \lambda d\lambda} \quad (1.1)$$

where  $f_\lambda(\lambda)$  is the flux density of the object. The predicted passband is then given by:

$$m_\lambda(P) = -2.5 \log(f_\lambda(P)) - m_0(P), \quad (1.2)$$

where  $m_0(P)$  is the zero-point magnitude of passband  $P$ , given by evaluating Equation 1.1 for a reference object. In the AB system this is a constant spectral flux density of 3631 Jy. In flux per unit wavelength this is:

$$\frac{f_\lambda(\lambda)}{\text{erg cm}^{-2} \text{ s}^{-1} \text{ \AA}^{-1}} = 0.1087 \left( \frac{\lambda}{\text{\AA}} \right)^{-2}. \quad (1.3)$$

In the Vega system, a spectrum of the A0V star Vega is used. Although the magnitude of Vega is by design zero in every passband, more recent measurements reveal a small magnitude offset. The Vega to AB magnitudes given in Table 1.1 assume Vega to have a magnitude 0.026.

### 1.2.3 Galactic extinction correction

*Ask Paul how this is done, how much of a difference it makes*

$A(u)$ , the Galactic extinction in the  $u$  passband at the position of the object, is given in the SDSS catalogue. It is computed using the maps of Schlegel, Finkbeiner, and Davis, (1998) and assuming a  $z = 0$  elliptical template. Quasar and galaxy SEDs have very different shapes in the optical/near-infrared region,

<sup>1</sup> <http://classic.sdss.org/dr7/algorithms/fluxcal.html>.

and therefore we re-derive the extinction corrections using a  $z = 1.5$  quasar SED template.

$A(u)$  is divided by 5.155 to give  $E(B - V)$ , the relative extinction between the B and V passbands (see table 6 in Schlegel, Finkbeiner, and Davis 1998). Conversions from the selective extinction  $E(B - V)$  to the total extinction  $A(\lambda)$  in each passband were calculated using a quasar SED template. These are given in the Table 1.1.

#### 1.2.4 Cross-matching SDSS to UKIDSS and WISE

There are 105 783 objects in the SDSS DR7 quasar catalogue. While WISE mapped virtually the entire sky, the UKIDSS footprint covers approximately one third of the SDSS footprint. 36 607 objects are cross-matched to the UKIDSS (with a  $2''$  matching radius) and WISE (with a  $3''$  matching radius) catalogues.

#### 1.2.5 Sample definition

We include only the 20 637 quasars with i passband magnitudes brighter than 19.1, i.e. the quasars selected by the main  $z < 3$  SDSS quasar selection algorithm  $z < 3$  (Richards et al., 2002). We verified that above the  $i = 19.1$  limit the sample is 95 per cent complete in all passbands. This suggests that our sample will not be biased towards quasars with redder spectra<sup>2</sup>. BAL quasars are excluded using the Allen et al., (2011) catalogue because the C IV line parameters of these quasars can not be reliably measured. This leaves 19 837 objects.

We further limit our sample to the redshift range  $1 < z < 3$ . Galaxy SEDs peak at  $\sim 1 \mu\text{m}$ , and fall away towards shorter wavelengths. On the other hand, AGN SEDs continues to increase short-ward of  $1 \mu\text{m}$ . As a result, the contrast between the AGN and galaxy luminosity increases as the redshift increases. Imposing a  $z = 1$  lower redshift limit on the redshift of our sample ensures that contributions to the SED from quasar host galaxies are negligible. The completeness of the SDSS DR7 quasar selection algorithm decreases steeply beyond  $z \sim 3$ , and this sets the upper redshift limit. The redshift and luminosity

*I don't fully understand this point*

<sup>2</sup> For a given i magnitude, a redder spectrum is more likely to be detected at longer wavelengths than a bluer spectrum.

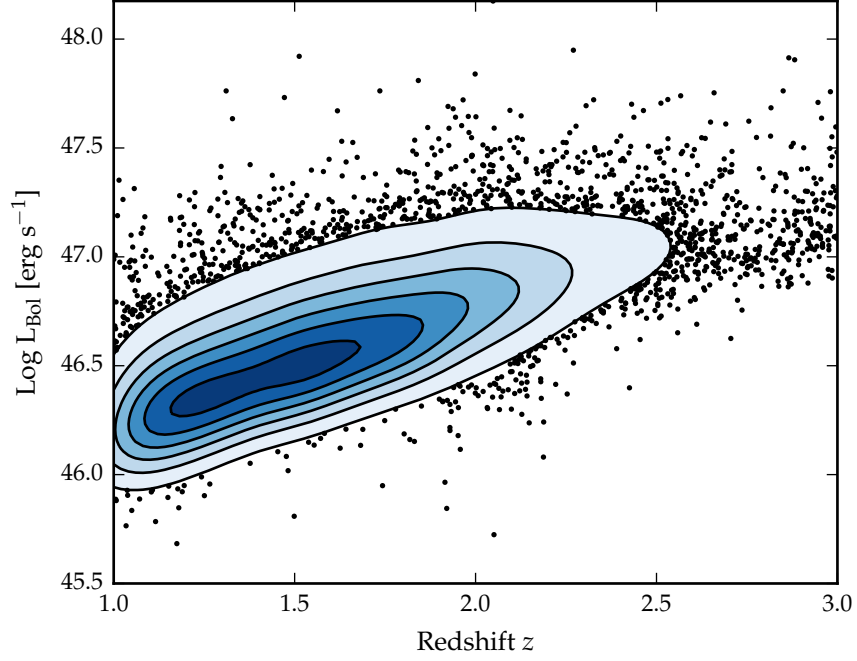


Figure 1.1: Distribution of our sample in the redshift-luminosity plane.

distribution of the final sample, containing 12 934 quasars, is shown in Figure 1.1.

### 1.3 CONSTRUCTING AN AGN SED MODEL

Since the physical processes that power AGN are generally understood only qualitatively, almost all AGN SED templates are empirical. The empirical template of Elvis et al., (1994) is still the most commonly cited, despite many additions and updates (e.g. Polletta et al., 2000; Kuraszkiewicz et al., 2003; Risaliti and Elvis, 2004; Richards et al., 2006; Polletta et al., 2007; Lusso et al., 2010; Shang et al., 2011; Marchese et al., 2012; Trichas et al., 2012). However, these composite spectra are often constructed from quasars with a huge range in luminosity as a function of wavelength. In addition, the presence of significant host galaxy at optical wavelengths in low-redshift objects is an additional complication which has not always been taken care of adequately. There is therefore a strong rationale for taking a parametric approach to modelling quasar SEDs. This the approach adopted in this work.

*Ask Paul for details  
on this.*

We construct an SED model that is valid between  $1216 \text{ \AA}$  and  $3 \text{ }\mu\text{m}$ . In this region the SED is dominated by the accretion disc, broad UV/optical emission-lines and thermal emission from the hottest ( $T \sim 1200\text{K}$ ) dust. In this Section, we describe how each of these components are represented in our parametric SED model. The effect of dust extinction at the AGN redshift is also incorporated into the model. At high redshifts,  $\text{Ly}\alpha$  forest absorption becomes significant. Because we do not attempt to model this effect, our model is valid only at wavelengths long-ward of  $1216 \text{ \AA}$ . We model dust emission using a single temperature ( $T \sim 1200 \text{ K}$ ) blackbody, which peaks at  $\sim 2 \text{ }\mu\text{m}$ . At longer wavelengths, emission from cooler dust farther from the central engine becomes increasingly important. We do not include this emission in our model, which restricts its validity to  $\lesssim 3 \text{ }\mu\text{m}$ . The model spectrum is shown in Figure 1.2, with each of the main components indicated.

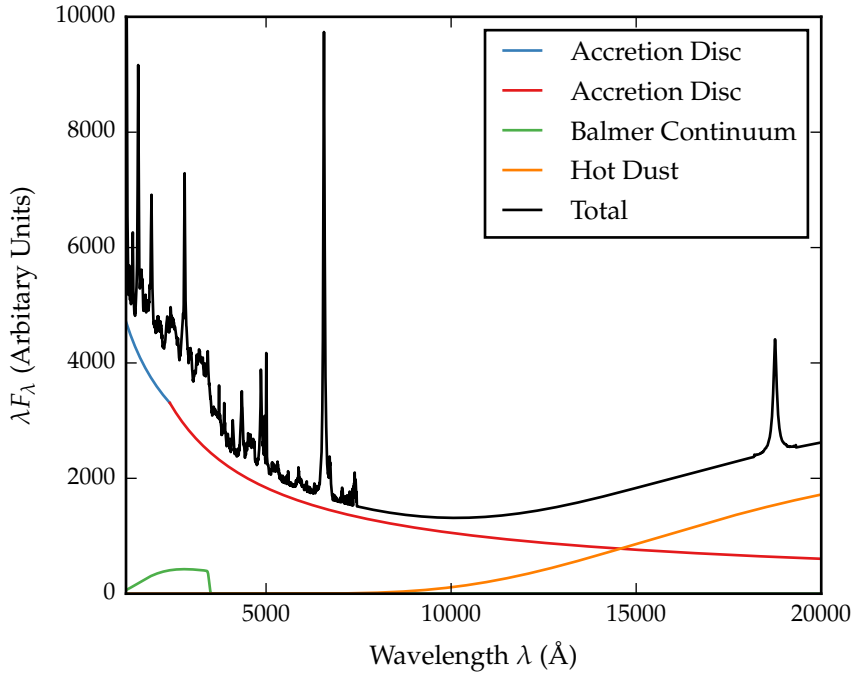


Figure 1.2: Model quasar spectrum at  $z = 1$ , showing the contributions to the total flux from the accretion disc, Balmer continuum, hot dust and emission lines.

### 1.3.1 Accretion disc

Thermal accretion disc emission in the  $0.1 - 1 \mu\text{m}$  region is characterised by a broken power-law with three free parameters: a break-wavelength,  $\lambda_{\text{break}}$ , a blue power-law index,  $\alpha_{\text{blue}}$ , for wavelengths shorter than the break wavelength, and a red power-law index,  $\alpha_{\text{red}}$ , for wavelengths longer than the break wavelength.

### 1.3.2 Balmer continuum

High order Balmer lines, optically thin Balmer continuum emission, two-photon emission and Fe II emission blend together to form the ‘Balmer’ continuum at  $\sim 3000\text{\AA}$ . We simulate the Balmer continuum using the empirical model given by Grandi, (1982):

$$F(\lambda) = C_{\text{BC}} \times B_{\lambda}(T_e)(1 - e^{-\tau_{\lambda}}); \quad \lambda \leq \lambda_{\text{BE}} \quad (1.4)$$

where  $C_{\text{BC}}$  is a normalisation factor,  $B_{\lambda}(T_e)$  is the Planck function,  $T_e = 13150\text{K}$  is the effective temperature,  $\lambda_{\text{BE}} = 3460\text{\AA}$  is the wavelength at the Balmer edge, and  $\tau_{\lambda} = \tau_{\text{BE}} (\lambda_{\text{BE}}/\lambda)^{-3}$  is the optical depth with  $\tau_{\text{BE}} = 45$  the optical depth at  $\lambda_{\text{BE}}$ . This function is convolved with a Gaussian with width  $\sigma = 5000\text{km s}^{-1}$  to simulate the effect of bulk velocity shifts comparable to those present in broad AGN emission-lines.

### 1.3.3 Hot dust

Thermal emission from hot dust, which dominates the SED at wavelengths longer than  $1 \mu\text{m}$ , is modeled using a blackbody

$$F_{\lambda} = C_{\text{BB}} \times \frac{2hc^2}{\lambda^5} \frac{1}{e^{\frac{hc}{\lambda k_B T_{\text{BB}}}} - 1}, \quad (1.5)$$

with two free parameters: the temperature  $T_{\text{BB}}$  and normalisation  $C_{\text{BB}}$  relative to the power-law continuum.

### 1.3.4 Emission-lines

We use an emission-line template taken from Francis et al., (1991), which has been extended by Maddox and Hewett, (2006)



to include the H $\alpha$  and Pa $\alpha$  emission-lines<sup>3</sup>. All emission-lines, with the exception of H $\alpha$  and H $\beta$ , are scaled using a single free parameter  $C_{\text{EL}}$ , which preserves relative EQWs:

$$F_{\lambda} = C_{\text{EL}} \times \frac{F_{\lambda,\text{el}}}{F_{\lambda,\text{cont}}} \times F_{\lambda} \quad (1.6)$$

where  $F_{\lambda,\text{el}}$  is the emission-line template,  $F_{\lambda,\text{cont}}$  is the continuum flux in the template, and  $F_{\lambda}$  is the continuum flux in the SED model. The redshifts and luminosities of the quasars contributing to the emission-line template change as a function of wavelength. To account for possible variations in the strengths of the different lines, H $\alpha$  and H $\beta$  are scaled separately:

$$F_{\lambda} = C_{\text{EL}} \times C_{\text{H}\alpha} \times \left( \frac{L(z)}{L(z_{\text{nm}})} \right)^{\beta} \times \frac{F_{\lambda,\text{el}}}{F_{\lambda,\text{cont}}} \times F_{\lambda}. \quad (1.7)$$

The luminosity dependence of the H $\alpha$  and H $\beta$  EQW (i.e. the Baldwin effect; Baldwin, 1977) is parametrised with a power-law with slope  $\beta = -0.04$ . The dependence of the mean AGN luminosity on redshift,  $L(z)$ , is determined empirically for the SDSS quasar catalogue.

### 1.3.5 Dust extinction

We simulate the effect of dust extinction at the quasar redshift using a custom extinction curve that is appropriate for the quasar population. To derive the quasar extinction curve, UKIDSS photometry was used to provide an  $E(B - V)$  estimate, via the magnitude displacement of each quasar from the locus of un-reddened objects. At redshifts  $2 < z < 3$  the reddening measure is made at rest-frame wavelengths  $3500 - 7000 \text{ \AA}$ , where Galaxy, LMC and SMC<sup>4</sup> extinction curves are very similar. The SDSS spectra of the same objects are then employed to generate an empirical extinction curve in the ultra-violet, down to  $1200 \text{ \AA}$ . The resulting curve has no  $2200 \text{ \AA}$  feature and rises rapidly with decreasing wavelength but is not as steep as the SMC curve. The extinction curve gives the colour excess  $E(B - \lambda)$  relative to the colour excess  $E(B - V)$  as a function

<sup>3</sup> The spectrum is not significantly different from the Vanden Berk et al., (2001) SDSS composite.

<sup>4</sup> LMC and SMC: Large and Small Magellanic Clouds.

of wavelength  $\lambda$ . The colour excess  $E(B - V)$  is related to the extinction in the V passband,  $A(V)$ , via the ratio  $R$ :

$$R_V = \frac{A(V)}{E(B - V)} \quad (1.8)$$

where we assume  $R_V = 3$ . Hence the extinction at a wavelength  $\lambda$   $A(\lambda)$  is

$$A(\lambda) = E(B - V) \times \left[ \frac{E(\lambda - V)}{E(B - V)} + R \right] \quad (1.9)$$

where the colour excess  $E(B - V)$  is a free parameter in our model. The attenuation of the flux at a given wavelength is then:

$$F_\lambda = F_\lambda 10^{-A(\lambda)/2.5} \quad (1.10)$$

in the rest frame of the quasar.

#### 1.4 DETERMINING OPTIMUM PARAMETERS FOR THE POPULATION

We begin by fitting a single SED model to all 19 853 quasars, encompassing a range of redshifts, luminosities, accretion rates etc. The free parameters in our model are summarised in Table 1.2. The reddening  $E(B - V)$  is fixed to zero, since a large fraction of SDSS quasars have very small amounts of dust reddening (Richards et al., 2003).

We divide the quasar sample into redshift bins from  $z = 1$  to  $z = 3$  in intervals of  $\Delta z = 0.1$ . In each redshift bin median passband magnitudes are calculated, and normalised such that  $i = 18$ . As described above, the SED model is valid between  $\sim 1200$  and  $30000 \text{ \AA}$ . We use the rizYJHKW1W2 passbands to constrain the model, which covers  $1550 - 23000 \text{ \AA}$  in the rest-frame. Model SEDs are generated at redshifts corresponding to the centres of the redshift bins. The SED model is shown at three different redshifts in Figure 1.3. Model magnitudes are calculated using Equations 1.1 and 1.2 and are normalised such that  $i = 18$ . We find the best-fitting model parameters by minimising the  $\chi^2$  statistic for the  $9 \times 21 = 181$  model and data magnitudes using the Nelder-Mead algorithm.

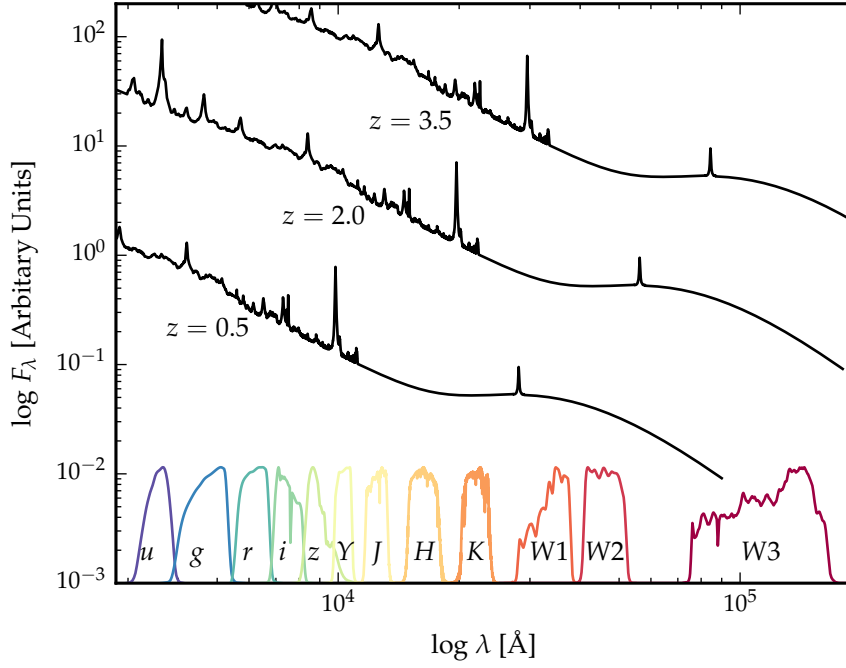


Figure 1.3: Model quasar spectrum at three different redshifts (each arbitrarily scaled), and throughput functions for SDSS, UKIDSS and WISE passbands.

Parameter	Symbol	Value
Blue power-law index	$\alpha_{\text{blue}}$	-0.478
Red power-law index	$\alpha_{\text{red}}$	-0.199
Power-law break	$\lambda_{\text{break}}$	2402
Blackbody temperature	$T_{\text{BB}}$	1306 K
Blackbody normalisation	$C_{\text{BB}}$	2.673
Emission-line scaling	$C_{\text{EL}}$	1.240
H $\alpha$ emission-line scaling	$C_{\text{H}\alpha}$	0.713
Balmer continuum scaling		0.135

Table 1.2: Best-fitting SED model parameters from fit to the median colours of quasars at redshifts  $1 < z < 3$ .

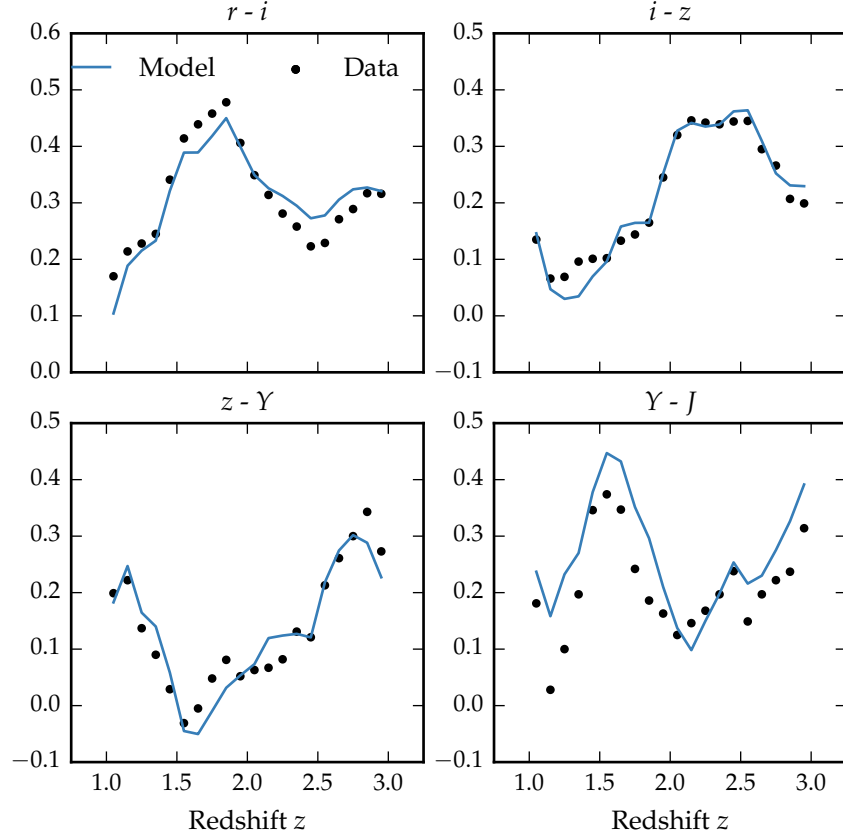


Figure 1.4: Median colours of quasars as a function of redshift and best-fitting SED model.

## 1.5 RESULTS - LESS GENERIC TITLE

The best-fitting parameters from the fit are shown in Table 1.2. The colours ( $r - i$ ,  $i - z$ , etc.) of the median SED, the and the best-fitting model are plotted as a function of redshift in Figure 1.4. Most of the large variations that can be seen in the median colours of the quasars as a function of redshift are due to strong emission-lines being redshifted into and out of the passbands.

In Figure 1.5 we show the data minus model residuals as a function of the rest-frame wavelength. The residuals indicate that over a large redshift range the model is effective able to reproduce the median observed colours of the sample. Discrepancies are at the  $< 0.1$  mag level. At a given rest-frame wavelength, there are no significant discrepancies between residuals in different passbands. This indicates that there is no significant evolution in the median SED as a function of redshift. We

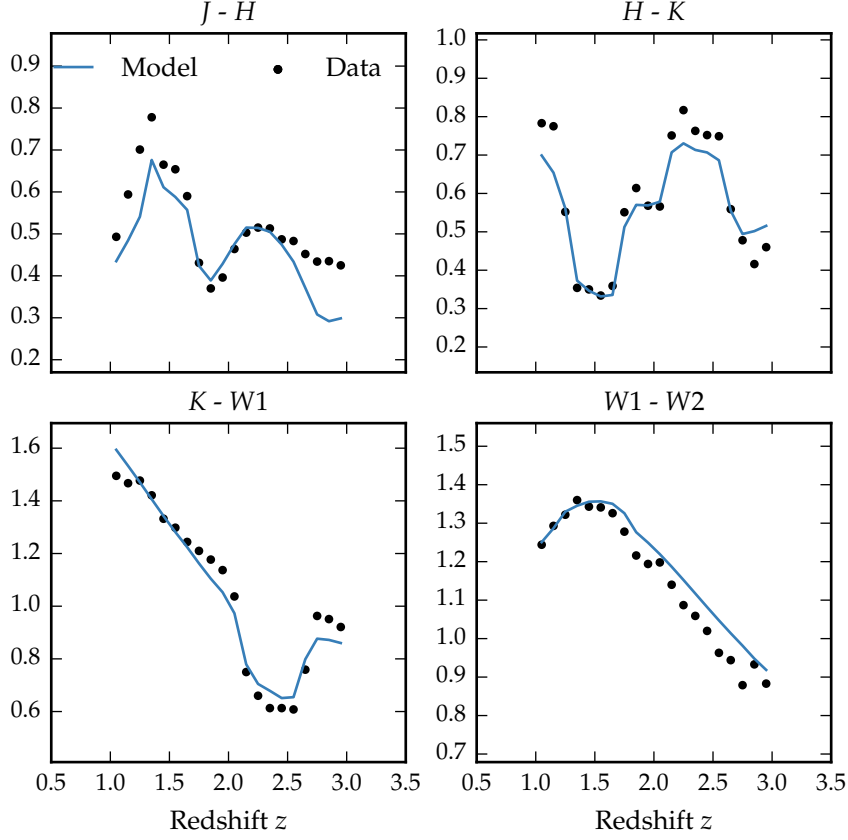


Figure 1.4: Continued.

conclude that a single, fairly simple parametric is effective at reproducing the median colours of tens of thousands of AGN with a large dynamic range in redshift and luminosity.

## 1.6 DIVERSITY OF HOT DUST PROPERTIES

In Figure 1.6 we plot the  $W1 - W2$  colours of the sample as a function of redshift at  $z < 3$ . At any given redshift we see a  $\sim 0.5$  mag dispersion in the  $W1 - W2$  colours. In this redshift range the  $W1$  and  $W2$  passbands are probing the  $1.2 - 2.8 \mu\text{m}$  and  $1.6 - 3.8 \mu\text{m}$  region of the rest frame SED respectively. The peak wavelength is at  $2.4 \mu\text{m}$  for a blackbody radiating at 1200 K. Therefore, the large spread in  $W1 - W2$  colours is highly suggestive of a range of hot dust properties in this sample.

We characterise the hot dust properties of our sample in terms of the temperature of the blackbody component and the near-infrared to ultra-violet luminosity ratio,  $R_{\text{NIR/UV}}$ . The

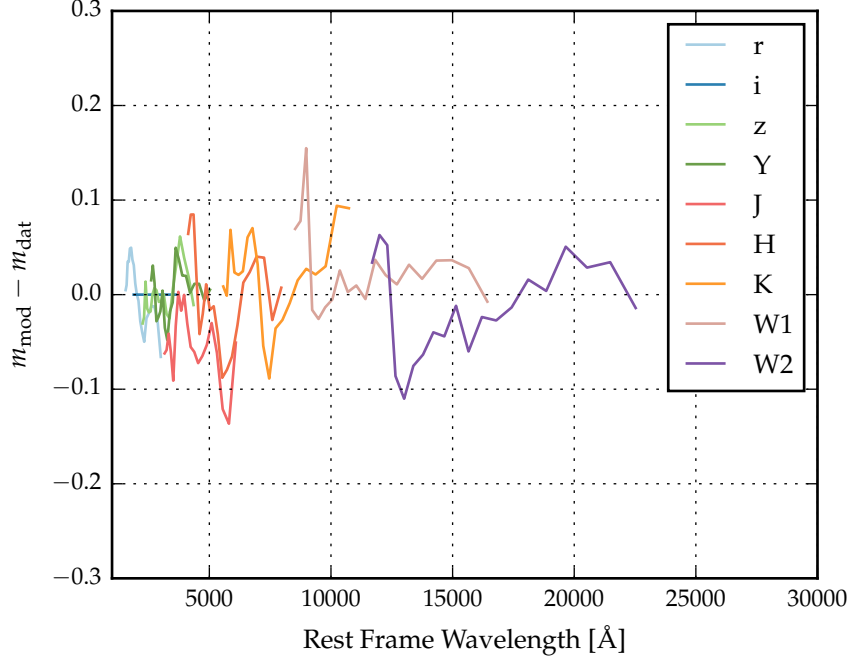


Figure 1.5: Residuals from fit as a function of rest-frame wavelength.

ultra-violet and near-infrared luminosities are calculated between 2000 and 9000 Å and 1 and 3  $\mu\text{m}$  respectively in the SED.

The temperature is likely related to the distance of the dust from the central engine. Dust that is closer in will be hotter, with the sublimation temperature of the dust grains setting the minimum radius. The value of  $R_{\text{NIR/UV}}$  is related to the covering factor of the hot dust. However, this simple interpretation is somewhat complicated by the fact that at large inclinations sight-lines to the hot dust may be obscured by cooler dust in the putative torus.

In Figure 1.6 we have plotted the W1 – W2 colours derived from our SED model with a fixed blackbody temperature (1306 K) and varying  $R_{\text{NIR/UV}}$ . The W1 – W2 colours indicate that the hot dust luminosity in this sample varies by a factor of  $\sim 5$ .

In the rest of this Chapter, we will measure hot dust parameters for individual quasars via SED fitting. We will characterise the range of hot dust properties present in the sample, and test its relation to quasar properties such as luminosity, black-hole mass and normalised accretion rate, and outflow-properties.

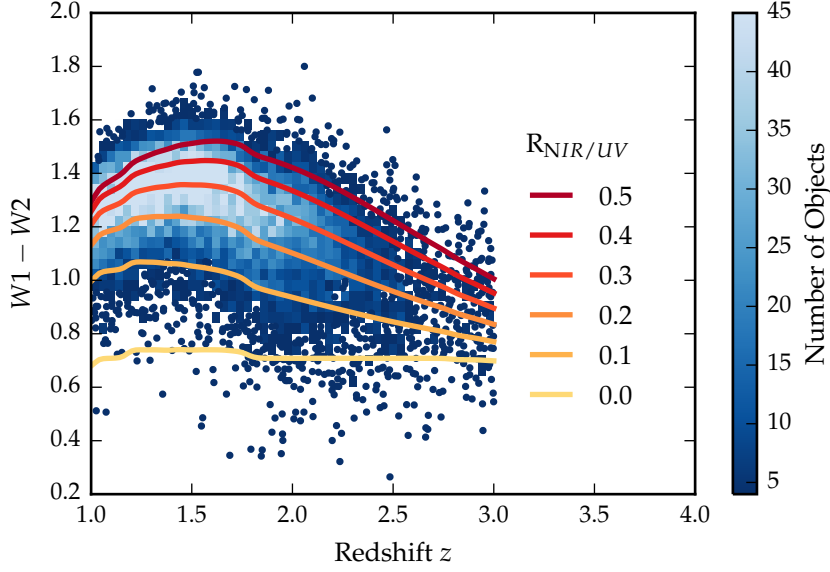


Figure 1.6:  $W1 - W2$  colours of sample as a function of redshift. Above a density threshold of four points per pixel points are represented by a two-dimensional histogram. On top we plot the colours of our standard SED model, with a fixed temperature and a varying near-infrared ( $1 - 3 \mu\text{m}$ ) to ultra-violet ratio.

#### 1.6.1 Defining a sample with uniform UV/optical properties

We limit our sample to 2329 quasars with redshifts  $2 < z < 2.7$ . At these redshifts, C IV emission is located within the wavelength coverage of the SDSS spectra. This will allow us to test the relationship between the hot dust and BLR outflow properties.

The shifting of passbands due to redshift limits the redshift range of the quasars for which hot dust properties can be reliably constrained. Constraining a  $T \sim 1200 \text{ K}$  blackbody component in the SED model requires photometric data covering  $\sim 1 - 3 \mu\text{m}$  in the rest-frame of the quasar. At redshifts  $2 < z < 2.7$   $W1W2W3$  is probing the  $0.9 - 4 \mu\text{m}$  region of the SED. Therefore the available data is sensitive to the hot dust component.

In general, care must be taken looking for trends with luminosity (and related properties including the BH mass and Eddington ratio) given the observed-frame passband information on the rest-frame SED can produce some strong systematics

with redshift. However, the redshift interval is narrow enough to prevent this from being a significant problem.

Holding the rest of the model parameters fixed, we will vary only the parameters of the blackbody. This requires the SED model to be reasonable fit to the quasar SEDs in the ultra-violet/optical region. In practice, this means excluding objects with extreme emission-line EQWs and/or significant dust extinction. We use the  $i - K$  colours of the quasars as a measure of the overall colour of the quasars as it provides the longest baseline in wavelength without being affected by absorption in the  $\text{Ly}\alpha$  forest at high redshifts. This is shown in Figure 1.7. A significant amount of the scatter in  $i - K$  can be attributed to intrinsic variations in the ultra-violet power-law slopes of the individual quasars, which is why we allow a negative ‘reddening’.

The SDSS and UKIDSS photometry are separated by 3 – 4 years in the source rest-frame. Therefore, some of the  $i - K$  scatter could be due to temporal variations in the brightness of the targets. However, the red-asymmetry of the  $i - K$  colours about the un-reddened SED model suggests that this effect is sub-dominant to intrinsic colour differences. However, there is a clear ‘red tail’ to the colour distribution which can be explained by dust reddening at the redshift of the quasar. We discarded from our sample quasars with  $i - K$  colours redder than our standard model with dust reddening  $E(B - V) = 0.075$  and bluer than  $E(B - V) = -0.075$  (Figure 1.7). Following this cut we are left with 2030 quasars in our high- $z$  sample.

### 1.6.2 *Fitting procedure*

We will fit a model to the individual quasar SEDs, allowing the temperature and normalisation of the black body component to vary. The model spectrum is redshifted to the redshift of the quasar being fit and passband magnitudes are calculated using Equations 1.1 and 1.2. We minimise the inverse variance weighted chi-squared statistic using the Levenberg-Marquardt algorithm. We impose a minimum error of 0.1 mag, corresponding to the model error for the medians colours (Figure 1.5). Data from  $ugrizYJHKW1W2W3$  is used in the model. However, to avoid  $\text{Ly}\alpha$  forest absorption, passbands are excluded if  $\lambda_{\text{eff}} < 1400\text{\AA}$ .



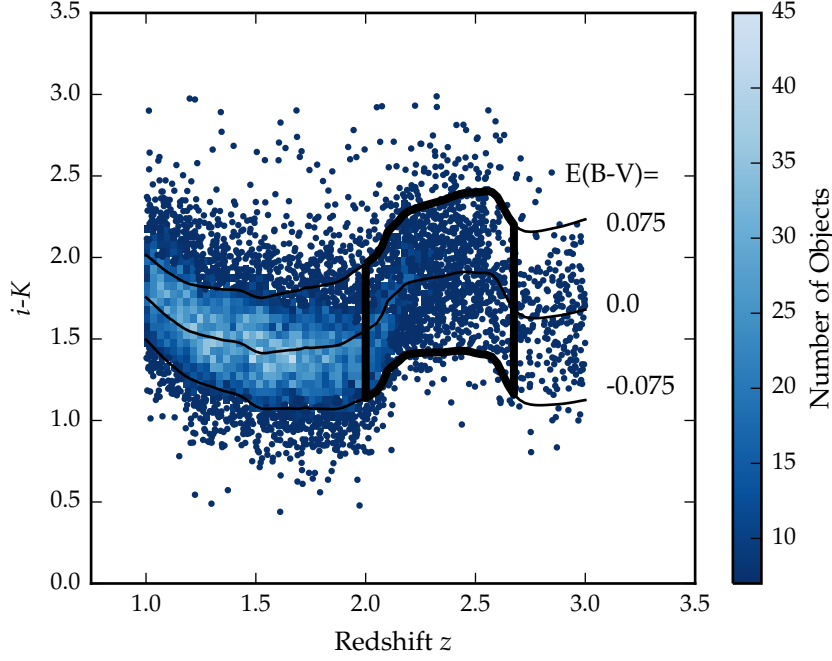


Figure 1.7:  $i - K$  colours of non-BAL DR7Q quasars with  $i > 19.1$  as a function of redshift. The lines show the colours of our model with varying amounts of dust extinction. Quasars with extinction  $|E(B - V)| > 0.075$  are excluded.

### 1.6.3 Distribution of hot dust parameters

The best-fitting hot dust temperature ( $T_{\text{BB}}$ ) and abundance ( $R_{\text{NIR/UV}}$ ) for the individual quasars are shown in Figure 1.8. Even after restricting the sample to have a relative narrow range of ultra-violet/optical SED shapes, we see significant diversity in the hot dust abundance, with the near-infrared ultra-violet luminosity ratio having a broad range from 0.1 to 0.6. The temperature takes on a relatively narrow range of values:  $1177 \pm 136$  K. This is consistent with the dust radius being set by the sublimation temperature of the dust grains.

We note a strong correlation between the temperature and  $R_{\text{NIR/UV}}$ . This is a result of the dependence of the blackbody peak on temperature and the fixed wavelength interval used to calculate the blackbody luminosity.

### Relationship between hot dust and BLR outflows

In this Section, we compare the hot dust parameters to the blueshift and EQW of the C IV emission. C IV blueshift measure-

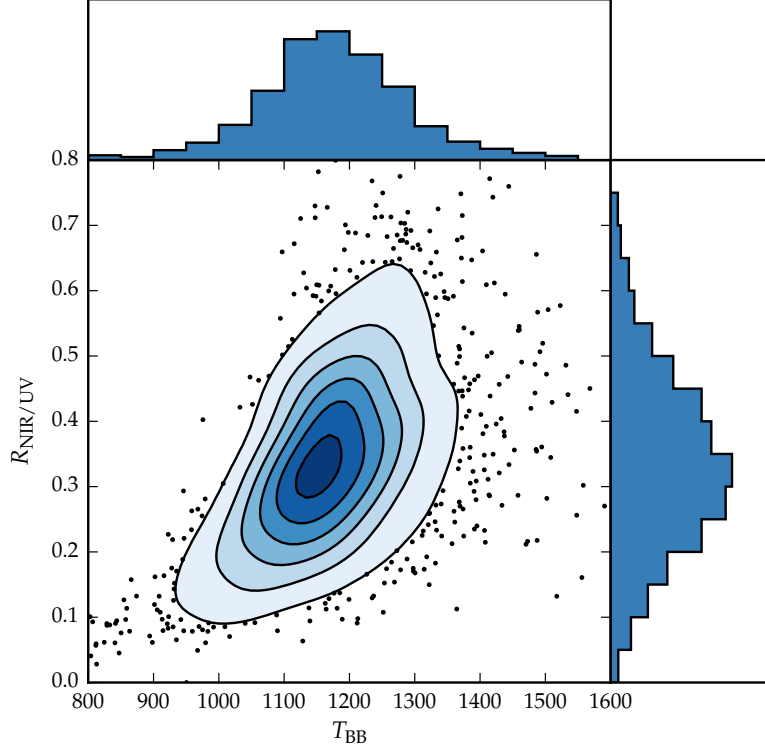


Figure 1.8: Histograms of the ratio of near-infrared to ultra-violet luminosity ( $R_{\text{NIR/UV}}$ ) and blackbody ( $T_{\text{BB}}$ ) and the correlation between these two parameters.

ments are described in Section ?? . The C iv blueshift is defined with respect to a systemic redshift measured by Allen & Hewett (2017, in preparation). This information is available for 98 per cent of the objects in our sample.

In Figure 1.9 we show that the near-infrared to ultra-violet luminosity ratio is correlated with the C iv blueshift. A similar result was recently reported by Wang et al., (2013). On the other hand, we find no correlations with the hot dust temperature.

The profiles of the emission-lines with large C iv blueshifts suggest that the BLR dynamics in these objects are dominated by high-velocity outflows. As we discussed at the beginning of this Chapter, outflows from further out in the accretion disc could contain significant amounts of dust. As the dusty wind is lifted above the accretion disc, it would be directly exposed to ultra-violet radiation from the inner accretion disc. Radiation pressure could efficiently accelerate the wind owing to the high cross-section of the dust grains (e.g. Fabian, 2012).

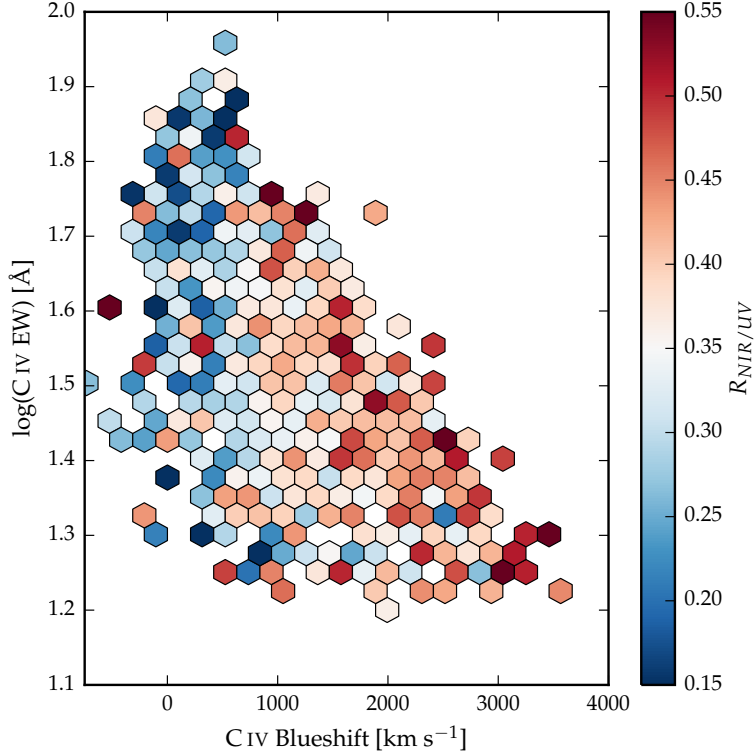


Figure 1.9: Rest-frame EQW and blueshift of the C IV line. The colours of the hexagons denote the median hot dust ( $T \simeq 1200$  K) abundance for all quasars at a given EQW and blueshift. Quasars with the most extreme outflow signatures are predominantly hot-dust rich.

Radiation pressure could flatten the geometry of the wind. The greater the radiation pressure, the flatter the geometry of the wind. This leads to a wider opening angle, which exposes more surface area that is viewable on a relatively face-on line of sight. This leads to the enhanced hot dust emission we observe in the quasars with high accretion rates and strong outflows.

A prediction of this model is an anti-correlation between the torus covering factor and the hot dust abundance. The torus covering factor would be reduced by the accretion disc wind, and this would increase the maximum inclination at which a type I quasar could be seen. This would mean direct sight lines to more of the dust closest to the accretion disc. Such a correlation has been identified by Roseboom et al., (2013).

At lower redshifts, Shen and Ho, (2014) have found that the hot dust properties are correlated with EV1. Shen and Ho, (2014) quantify the relative torus emission using the  $r - W1$  colour for a sample of  $0.4 < z < 0.8$  SDSS quasars. At these

redshifts W1 is observing between 1.9 and 2.4  $\mu\text{m}$  in the rest-frame of the quasar, which suggests that they are sensitive to the same component of hot dust which we are investigating. Shen and Ho, (2014) also find that torus emission is enhanced in quasars with larger  $R_{\text{FeII}}$ . They suggests that this may be caused by more efficient disc winds that facilitate the formation of a dusty torus.

#### 1.6.4 Correlations with quasar properties

The distribution of blackbody temperatures is relatively narrow  $\sim 200$  K and so, as expected, we do not observe any correlations between the temperature and other quasar properties. Correlations between the hot dust abundance  $R_{\text{NIR/UV}}$  and the ultra-violet luminosity, BH mass and Eddington ratio are shown in Figure 1.10.

The ultra-violet luminosity is measured at 1350  $\text{\AA}$  in the spectral modelling done by Shen et al., (2011). We do not observe any correlation between  $R_{\text{NIR/UV}}$  and the ultra-violet luminosity (Figure 1.10a). However, the dynamic range in luminosity is small in this sample ( $\sim 1$  dex) because of the restricted redshift range.

In Figure 1.10b we show  $R_{\text{NIR/UV}}$  as a function of the BH mass. Masses are C IV FWHM-based single-epoch virial estimates, as computed by Shen et al., (2011).  $R_{\text{NIR/UV}}$  is positively correlated with the BH mass; the Spearman correlation coefficient,  $\rho_s$ , is 0.26. However, in the previous Section, we found  $R_{\text{NIR/UV}}$  to be correlated with the C IV blueshift and, in Chapter ??, we demonstrated that BH masses are severely overestimated in quasars with large C IV blueshifts. We therefore predict that the apparent correlation between  $R_{\text{NIR/UV}}$  and the BH mass is due to systematic biases in the C IV-based masses. We can test this by comparing  $R_{\text{NIR/UV}}$  with BH mass estimates which have been corrected using the prescription described in Chapter ?? (Figure 1.10d). As expected, the correlation vanishes ( $\rho_s = 0.07$ ). A similar result is found when  $R_{\text{NIR/UV}}$  is compared to the Eddington ratio, which is inversely proportional to the BH mass. Using masses from Shen et al., (2011) an anti-correlation is observed between  $R_{\text{NIR/UV}}$  and the Eddington ratio ( $\rho_s = -0.36$ ; Figure 1.10c) but this disappears when corrected masses are employed ( $\rho_s = -0.12$ ; Figure 1.10e). This demonstrates how using conventional BH mass estimates based on C IV can lead to spurious correlations with other quasar

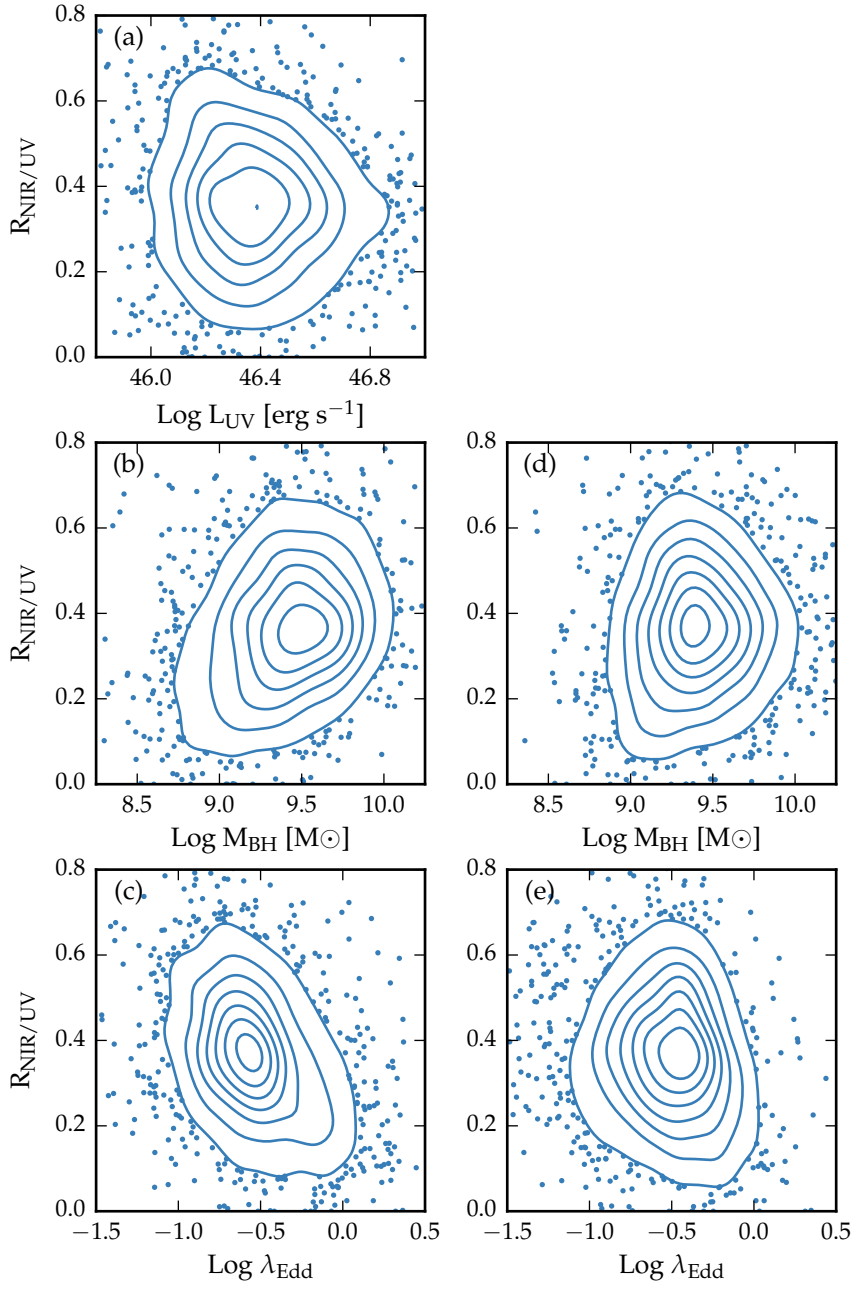


Figure 1.10: Best-fit near-infrared to ultra-violet luminosity ( $R_{\text{NIR/UV}}$ ) as a function of ultra-violet luminosity, BH mass and Eddington ratio. In (b) and (c) BH mass estimates, which are based on the C iv FWHM, are taken from Shen et al., (2011). In (d) and (e) BH mass estimates have been corrected using the procedure described in Chapter ?? . Using the corrected masses the correlations between  $R_{\text{NIR/UV}}$  and the BH mass and Eddington ratio are significantly reduced.

properties, but that this can be avoided using the improved mass estimates presented in Chapter ??.